

PAPER

## Assessment of the application of paratellurite for the acousto-optical deflection of terahertz rays based on broadband spectroscopy data

To cite this article: Gennadiy Komandin *et al* 2020 *J. Phys. D: Appl. Phys.* **53** 495102

View the [article online](#) for updates and enhancements.



**IOP | ebooks™**

Bringing together innovative digital publishing with leading authors from the global scientific community.

Start exploring the collection—download the first chapter of every title for free.

# Assessment of the application of paratellurite for the acousto-optical deflection of terahertz rays based on broadband spectroscopy data

Gennadiy Komandin<sup>1</sup> , Vadim Nozdrin<sup>1</sup>, Sergey Chuchupal<sup>1</sup>, Vladimir Lomonov<sup>2</sup>, Yurii Pisarevskii<sup>2</sup>, Oleg Porodinkov<sup>1</sup> and Igor Spector<sup>1</sup>

<sup>1</sup> Prokhorov General Physics Institute of the Russian Academy of Sciences, Vavilov str. 38, Moscow 119991, Russia

<sup>2</sup> FSRC «Crystallography and Photonics» of the Russian Academy of Sciences, Leninskiy Prospekt 59, Moscow 119333, Russia

E-mail: [gakomandin@mail.ru](mailto:gakomandin@mail.ru)

Received 10 March 2020, revised 8 July 2020

Accepted for publication 17 August 2020

Published 16 September 2020



CrossMark

## Abstract

The rapid spatial guidance of terahertz (THz) radiation is a key problem in modern THz spectroscopy and imaging. Single-crystal  $\alpha$ -TeO<sub>2</sub> has advanced optical and elastic characteristics. This crystal widely used in acousto-optical devices in the visible and near-infrared (IR) ranges. Its application in the THz frequency range at temperatures of approximately 300 K is limited by high radiation absorption. We studied the electrodynamic characteristics of a paratellurite crystal in a wide frequency region at temperatures ranging from 77 to 300 K using pulsed broadband THz spectroscopy and IR Fourier spectroscopy. The temperature evolution of the complex refractive index, as well as the impact of phonon contributions and second-order processes on the absorption of radiation for polarisation along the crystallographic directions of [001] and [110], was evaluated. It was determined that at temperatures below 100 K, intrinsic absorption processes are significantly suppressed, which is mainly caused by a decrease in first- and second-order phonon contributions. The temperature dependencies of the refraction index and absorption coefficient of paratellurite in the THz range were obtained. We demonstrate that crystal cooling leads to a shift in the high-frequency boundary of the deflected THz radiation from 15 to 40 cm<sup>-1</sup> along the [001] crystallographic axis.

Keywords: terahertz and infrared spectroscopy, dielectric and acousto-optic parameters, deflection of the terahertz radiation

(Some figures may appear in colour only in the online journal)

## 1. Introduction

Terahertz (THz) waves ( $f \sim 0.1\text{--}3$  THz,  $\nu \sim 3\text{--}100$  cm<sup>-1</sup>,  $\alpha \sim 1\text{--}0.1$  mm) have a number of advantages compared to higher-frequency types of radiation, such as ultraviolet radiation and X-rays. These advantages include very low (almost absent) ionising ability, which facilitates the study of highly sensitive biological objects. THz radiation has a longer

wavelength than infrared (IR) and visible radiation, which reduces the resolution of THz imaging systems. However, this resolution can be significantly improved by using solid immersion [1, 2].

Furthermore, longer wavelengths are less scattered by the spatial heterogeneities of multicomponent media. Methods for determining the spatial distributions of components and their mutual concentrations are in high demand in various fields,

including pharmacology [3–5], biology [6], and medicine [7, 8]. Typically, the spatial distribution of the electromagnetic characteristics of an object is observed by moving the test sample relative to a THz beam [2]. However, this approach is not always practical, particularly when THz radiation is used for medical purposes, such as the intraoperative diagnosis of malignant neoplasms [10]. Improving the speed of THz imaging systems entails both the development of high-rate broadband and quasimonochromatic emitters and detectors for radiation, as well as the development of fast scanning systems [9].

Mechanical and optical deflectors are used to scan fixed samples. In addition to micromechanical scanners [11], acousto-optical devices in which diffraction effects determine changes in the direction of propagation of THz radiation [12] have shown significant promise. Acousto-optical deflection is based on spatial changes in the refractive index of a substance generated by ultrasonic waves. To assess the potential of acousto-optical effects, the necessary parameters are the elastic constants and optical parameters of the corresponding crystal. The elastic constants used for calculating diffraction efficiency are independent of the wavelengths of deflected beams. The complex refractive indices  $N = n + ik$  in the directions of ordinary  $N_o$  and extraordinary  $N_e$  rays, as well as the absorption coefficient of the medium  $\alpha = 4\pi k/\lambda$ , are the optical parameters required for calculating acousto-optical efficiency. Here,  $k$  is the extinction coefficient and  $\lambda$  is the wavelength. The relationship between the refractive index and the stress produced by an acoustic wave is determined by the photoelasticity tensor, which can be considered as a scalar  $1/n^2 = p_{eff}S$  for a major crystallographic direction, where  $S$  is the stress along the chosen crystallographic direction. The electrodynamic parameters of materials in the THz and visible spectral regions differ significantly based on the contributions of IR phonon modes.

The deflection of THz radiation using acousto-optical methods was demonstrated in [13]. The swing angle of the THz radiation of a free electron laser with a wavelength of  $140 \mu\text{m}$  was calculated to be in the range of  $2.5^\circ$ – $3^\circ$  by using a Ge crystal as an acousto-optical medium. The diffraction efficiency  $I_{diff}/I_0$  was  $0.05\%$  at a control ultrasound power level of  $1 \text{ W}$ , where  $I_{diff}$  and  $I_0$  are the intensities of the diffracted and incident beams, respectively.

The diffracted beam intensity can be estimated from the following relationship:

$$I_{diff} \approx I_0^* \frac{\pi^2}{2\lambda^2} \frac{M_2 P_{ac}}{D} l \cdot Tr, \quad (1)$$

where  $\lambda$  the wavelength of light and  $l$  is the length of the acousto-optical interaction. The ultrasonic power  $P_{ac}$ , beam diameter  $D$ , and transmittance  $Tr$  of the crystal (accounting for Fresnel reflection) are determined by the experimental conditions and choice of material.

From (1), one can see that efficiency decreases as the square of the wavelength. The corresponding wavelengths for THz frequencies lie in the range of  $100 \mu\text{m}$  to  $1 \text{ mm}$ , which are approximately four orders of magnitude greater than the wavelengths of visible light. Decreases in efficiency are also affected by the length of the acousto-optical interaction

$l = l/\alpha$ , where  $\alpha$  is the absorption coefficient. However, diffraction efficiency also depends on the acousto-optical figure of merit  $M_2$ , which is determined by the sixth power of the refractive index as  $M_2 = n^6 p^2 / \rho v^3$ , where  $\rho$  is the density of the media and  $v$  is the acoustic wave phase velocity. According to the data [13] for single-crystal Ge ( $n = 4$  in the THz range at  $T = 300 \text{ K}$ ), the parameters described above can be estimated as  $M_2 \sim 180 \cdot 10^{-15} \text{ s}^3 \text{ kg}^{-1}$  and  $\alpha \sim 0.75 \text{ cm}^{-1}$  for  $\lambda = 140 \mu\text{m}$ . Therefore, materials with large refractive indexes and minimal absorption coefficients are desirable for the acousto-optical deflection of THz waves.

Paratellurite, which is widely used as an acousto-optical crystal in the visible and near-IR ranges, is one such materials. Its refractive index and absorption coefficient at  $300 \text{ K}$  were determined for the THz range in [14, 15]. Recently, the optical characteristics of paratellurite were measured in the IR and THz ranges [16] for a particular interaction geometry. Assessment of the acousto-optical figure of merit  $M_2$  was conducted using the dispersionless approximation. The relatively low phase velocity of ultrasonic waves in paratellurite ( $v_{us} \sim 3.5 \cdot 10^3 \text{ m s}^{-1}$ ) makes this crystal advantageous compared to Ge ( $v_{us} \sim 5.6 \cdot 10^3 \text{ m s}^{-1}$ ) [13]. However, phonon absorption narrows the frequency range for the acousto-optical application of this crystal in the THz range, whereas this factor is irrelevant for Ge.

Paratellurite is one of the three known forms of tellurium oxide [17].  $\alpha$ -TeO<sub>2</sub> has a tetragonal structure  $D_4^4 P4_12_12$  and contains four formula units per cell [18, 19]. Factor group analysis of lattice vibrations in the  $P4_12_12$  structure yields the following phonons:  $\Gamma_{P4_12_12} = 4A_1 \oplus 4A_2 \oplus 5B_1 \oplus 4B_2 \oplus 8E$ . The IR active phonons are  $4A_2$  and  $8E$ . The crystal  $\alpha$ -TeO<sub>2</sub> has nonlinear and piezoelectric properties [20]. The acousto-optical properties of paratellurite were investigated in [21–23]. This material is widely used to fabricate various acousto-optical devices for the wavelength range of  $0.35$ – $5 \mu\text{m}$ . Additionally, the potential of generating THz radiation using paratellurite crystals exposed to femtosecond laser pulses was demonstrated in [15]. In such emitters, there is no photoexcitation of free charge carriers, which increases the absorption of THz radiation in photoconductive semiconductor antennas.

In the THz range, radiation losses are caused by both intrinsic [24] and extrinsic [25] mechanisms. The latter are determined by external factors, primarily defects, and can be minimised by improving sample synthesis technology [26]. Intrinsic mechanisms are a consequence of the interactions between radiation and a crystal lattice. The interaction between radiation and isolated phonon IR active modes is described by the harmonic oscillator model. The weak influence of anharmonicity is accounted for by the damping coefficient. In general, the damping coefficient is a function of frequency and temperature [27]. However, frequency dependence is typically neglected because it is limited to a relatively small frequency range near the resonant frequency. Therefore, the main factor determining changes in the shape of the absorption line of the optical phonon mode and its dispersion in the THz range is the temperature dependence of the damping coefficient. Approximation of the isolated phonon mode becomes biased for crystals with large numbers of IR active phonon

modes. In such cases, one should use a model that considers the interactions between modes [28]. The temperature dependence of complex coupling coefficients also affects the dispersion of absorption in the THz range.

The optical  $n$ ,  $k$ , and electrodynamic  $\varepsilon'$ ,  $\varepsilon''$  characteristics of paratellurite in the THz spectral region differ significantly from those in the visible and near-IR ranges. Changes in the refractive index and absorption coefficient in the THz range are determined by contributions from the optical phonon modes. The absorption lines of phonon modes are located in the far-infrared (FIR) range. Therefore, they affect the dispersion of the optical parameters of crystals in the THz range. In this manner,  $\alpha$ -TeO<sub>2</sub> differs from Ge [29], whose optical characteristics in the visible and near-IR ranges can be used to evaluate its acousto-optical efficiency in the THz range.

In addition to first-order processes with photon absorption and optical phonon excitation, in the THz range, there are also many-particle high-order processes that increase total absorption by at least an order of magnitude [30–33]. The absorption of radiation by a phonon on the Brillouin zone boundary leads to the transition of that phonon to a higher energy branch. This process exhibits significant temperature dependence. The energy of the absorbed photon is determined by the energy difference between phonon branches. The occupation numbers of phonon branches determine the phonon transition probability, meaning they also determine the absorption value for radiation. According to [30], the temperature dependence of  $\alpha(T)$  determined by the difference between two states, which depends on the occupation number in each state  $\eta_i = (e^x - 1)^{-1}$ , where  $x = \hbar \omega_i / k_B T$ , and  $\alpha(T) \sim \eta_1 - \eta_2 = \frac{x e^x}{(e^x - 1)^2} \frac{\omega}{\omega_1}$ , where  $\hbar$  is the Planck constant,  $k_B$  is the Boltzmann constant, and  $\omega$  is the circular frequency.

The laws of conservation of energy and momentum limit the potential for such transitions. The conditions for the equality of phase velocities and phonon polarisations must be satisfied to facilitate transitions between phonon branches [31, 32]. These processes contribute to the absorption by several orders of magnitude less than first-order phonon absorption, so they are often neglected. However, there are many problems for which considering high-order processes is of fundamental importance in terms of accuracy and reliability [34–36].

The goal of this work was to evaluate the prospects of using paratellurite crystals for the acousto-optical deflection of THz rays. Our study focused on the analysis of the temperature dependencies of wide-band experimental spectra in the THz-IR region, which were measured along the propagation directions of ordinary and extraordinary rays. Knowing the temperature dependencies of electrodynamic parameters obtained in the THz range makes it possible to separate the contributions of the various intrinsic mechanisms that determine the electrodipole absorption of THz radiation.

## 2. Experiments

### 2.1. Sample preparation

High-quality, defect-free paratellurite single crystals with 40-mm diameters and 40-mm lengths along the [110] direction

were grown using the weight-controlled Czochralski method with a platinum crucible and resistance heating. The raw material was TeO<sub>2</sub> powder with an impurity content less than 1 ppm. The crystals were oriented using X-ray diffraction and cut along the [110] and [001] directions to a typical size of approximately 10 × 10 mm. The thickness of the plane-parallel plate  $\alpha$ -TeO<sub>2</sub> crystals was measured to be  $624 \pm 2 \mu\text{m}$ . The high-quality optical surfaces were polished.

### 2.2. Spectroscopic technique

The transmission and reflection spectra of paratellurite single crystals in the range of 8–5000 cm<sup>-1</sup> were measured using three complementary spectrometers. Low-frequency calibration measurements in the range of 8–12 cm<sup>-1</sup> were performed at 300 K using a sub-millimetre coherent spectrometer with a source of quasimonochromatic frequency-tuneable radiation based on backward wave oscillator (BWO) [37, 38].

Transmission spectra in the THz range were measured using a laboratory broadband pulsed time-domain spectrometer (TDS) [39]. We used a long scanning length and Tukey apodization function with a wide window for detecting the first ballistic pulse and satellites. This allowed us to reconstruct the interference patterns in the transmission spectra and calibrate the THz TDS spectra using the low-frequency data from BWO spectroscopy. TDS yields reliable measurements in the frequency range of 10–90 cm<sup>-1</sup> with a spectral resolution of 0.2 cm<sup>-1</sup>. Freestanding wire grids were used as polarisers in both spectrometers for the formation of linearly-polarised radiation. The wire diameter was 8  $\mu\text{m}$ . The grids had a period of 25  $\mu\text{m}$ , which is shorter than the shortest wavelength of  $\lambda = 100 \mu\text{m}$  used in the THz range [40]. The polarisation degree, which is defined as a ratio of the magnitude of a signal passing through a pair of crossed polarisers to that of a signal passing through parallel oriented polarisers was no less than 0.99 in the entire spectral range. Measurements using BWO and THz spectrometers were performed with two grids acting as a polariser and analyser, which were installed before and after the sample position, respectively.

The reflectivity and transmissivity spectra in the FIR and middle-IR (MIR) ranges were measured using an IR Fourier spectrometer (Bruker IFS-113 v). A Globar and Hg lamp were used as sources of IR radiation in the MIR and FIR ranges, respectively. The spectral resolution was 2 cm<sup>-1</sup> over the range of 30–5000 cm<sup>-1</sup>. A metal periodic structure with 1200 lines per millimetre deposited on a 60- $\mu\text{m}$ -thick polyethylene film was used as a polariser in the IR range. A preliminary aligned polariser was installed in front of the sample position. Reflecting and refracting optics were used to focus the THz and IR radiation. The spot size was approximately 4 to 6 mm. Plane wave approximation (in caustic) was performed based on the configuration of the optical systems of the spectrometers. The angle of incidence on the sample did not exceed 6°. Therefore, measurements of the reflectivity spectra were performed using s-polarisation. A polished silver plate was used as a reference mirror.

For measurements at low temperatures, a laboratory flow optical cryostat with a sample orientation unit was adopted

[41]. Temperature was controlled using a platinum thermometer and stabilised by an integral heater and flow regulator for refrigerant with an accuracy of  $\pm 1$  K per measurement cycle. The cryostat windows consisted of 10- $\mu\text{m}$ -thick polyethylene films, which minimised THz radiation loss. The sample was attached to a movable holder with an aperture diameter of 8 mm. To reduce the pressure difference inside and outside the cryostat during the evacuation of the TDS and IR spectrometers, the internal volume of the cryostat was connected to the volumes of the spectrometers. After reaching the required vacuum and during the process of measuring spectra, evacuation of the cryostat and spectrometer was conducted separately. A Thyracont VD85 vacuum meter was used to monitor the residual pressure.

### 2.3. Spectra analysis

The spectra of complex dielectric permittivity were derived from the experimental transmission and reflection spectra using the Fresnel equations and dispersion analysis. The reflectivity spectra in the range of the phonon resonances were fitted by minimising the mean squared deviation of the calculated and experimental spectra as follows:

$$R(\nu) = \left| \frac{\sqrt{\varepsilon(\nu)} - 1}{\sqrt{\varepsilon(\nu)} + 1} \right|^2.$$

The dispersion of the reflectivity spectra was fitted using the factorised four-parameter (semi-quantum) generalised oscillator model [42–46] as follows:

$$\varepsilon(\nu) = \varepsilon_\infty \prod_{j=1}^N \frac{\nu_{jLO}^2 - \nu^2 + i\nu\gamma_{jLO}}{\nu_{jTO}^2 - \nu^2 + i\nu\gamma_{jTO}}. \quad (2)$$

This model has four adjustable parameters, namely the transverse and longitudinal frequencies ( $\nu_{jLO}$  and  $\nu_{jTO}$ , respectively) and transverse and longitudinal damping constants ( $\gamma_{jLO}$ ,  $\gamma_{jTO}$ , respectively), where  $\varepsilon_\infty$  is the high-frequency dielectric constant. The dielectric permittivity of tetragonal  $\alpha$ -TeO<sub>2</sub> should be considered as a tensor [47]. We used equation (2) to determine the optical phonon mode parameters based on the reflectivity spectra along the [001] and [110] crystallographic axes. These spectra were obtained under linear polarised IR radiation. Therefore, equation (2) could be applied in scalar form.

The contribution of each mode to the dielectric permittivity  $\Delta\varepsilon_j$  was determined using the following relationship [48–50]:

$$\Delta\varepsilon_j = \varepsilon_\infty \frac{\nu_{jLO}^2 - \nu_{jTO}^2}{\nu_{jTO}^2} \prod_{k \neq j} \frac{\nu_{kLO}^2 - \nu_{jTO}^2}{\nu_{kTO}^2 - \nu_{jTO}^2}. \quad (3)$$

The LO frequencies of the optical phonon modes can be calculated using the dielectric loss function. For small values of the damping constant, zeros in the dielectric response correspond to the maxima of the following function [51]:

$$\text{Im} \left( \frac{1}{\varepsilon^*(\nu)} \right) = \frac{\Delta\varepsilon}{\varepsilon_0 \varepsilon_\infty} \frac{\nu_{TOj}^2 \gamma_{TOj} \nu}{(\nu_{LOj}^2 - \nu^2) + \gamma_{TOj}^2 \nu^2}, \quad (4)$$

where  $\varepsilon_0$  is the static dielectric constant.

The experimental reflectivity spectra also were fitted using the classical oscillator model to compare the resulting parameters with the data [52] as follows:

$$\varepsilon^*(\nu) = \varepsilon_\infty + \sum_{j=1}^N \frac{\Delta\varepsilon_j \nu_j^2}{\nu_j^2 - \nu^2 + i\nu\gamma_j}, \quad (5)$$

where  $\nu_j$  and  $\gamma_j$  are the Eigenfrequency and damping constant of the  $j$ th (TO) mode, respectively.

### 3. Results and discussion

There are two basic intrinsic mechanisms leading to absorption of THz radiation. Previous studies [33, 53] have shown that second-order absorption processes make a significant contribution at temperatures above 80 to 100 K. To determine the contributions of these processes, it is necessary to determine the first-order phonon absorption in the THz range. The contribution of phonon absorption in the THz range was calculated by fitting the Reststrahlen bands in the reflectivity spectra in the IR range.

The experimental and calculated reflectivity spectra for the [001] direction at 77 and 300 K are presented in figures 1(b) and (d), respectively. The absorption in the polyethylene windows of the cryostat and the substrate of the polariser distort the spectra, resulting in spikes in the narrow bands at approximately 750, 1500, and 2700 to 3000  $\text{cm}^{-1}$ . There are discrepancies between the experimental data and fitted data in the area below 70  $\text{cm}^{-1}$  for both polarisations and in the range of 120–200  $\text{cm}^{-1}$  for the polarisation E||[001]. The distortions in the experimental data are caused by non-resolved interference pattern in the transparency ranges of the sample based on the insufficient coherence length of the sources and low spectral resolution (sampling theorem) [54–56]. Another feature of the experimental reflectivity spectra is upshifted high-frequency regions caused by additional incoherent reflections from the backside of the sample. Corresponding data for the [110] direction are presented in figure 2.

Earlier in [52], the parameters of these modes were determined using a classical oscillator model for temperatures of 300 and 80 K.

We will first discuss the impact of the absorption of optical phonon modes on the temperature evolution of the transmissivity spectra in the THz range. Based on the data presented in figure 1, it can be concluded that the A<sub>2</sub>(1)TO mode has the greatest influence on the spectra in the THz range. The A<sub>2</sub>(2) mode is located substantially higher in the frequency range and its contribution to the absorption in the THz range can be considered to be negligible. Figure 2 presents the data for the [110] direction. The first mode E(1) provides a small dielectric contribution. The mode E(2) is close in frequency to E(1) and has a dominant contribution that exceeds the contribution of the first mode. Therefore, to estimate absorption in this case, the temperature dependencies of the frequencies and damping constants of both E(1) and E(2) must be considered.

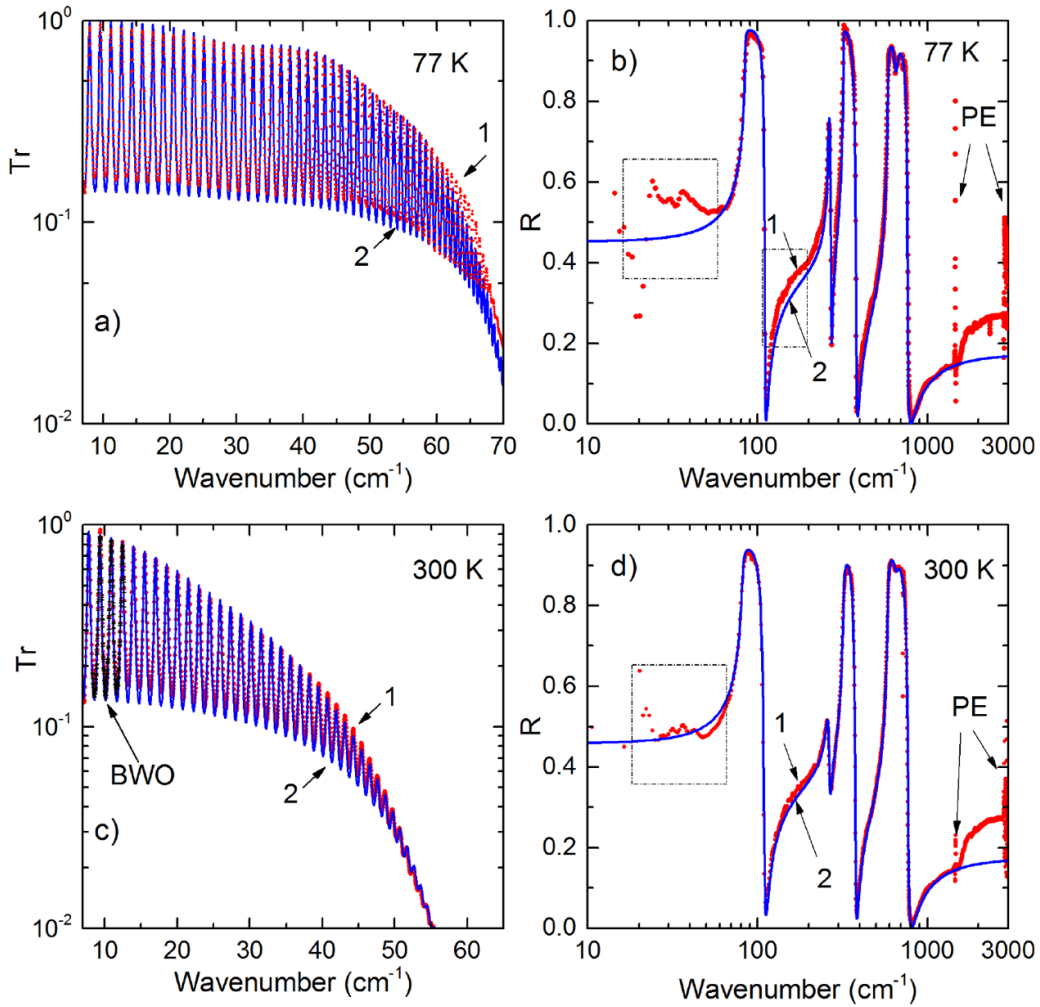


**Figure 1.** (a), (c) Transmissivity and (b), (d) reflectivity spectra of paratellurite single crystals for the electric field vector of THz radiation  $\mathbf{E}||[001]$  at 77 and 300 K. Experimental data: points. Calculation results: lines. Dash-dotted rectangles represent areas where the experimental reflectivity spectra are distorted. (b), (d) Spikes caused by absorption lines in the polyethylene windows. The reflected intensity detected by the spectrometer in the spectral region above  $1500\text{ cm}^{-1}$  contains contributions from the IR radiation source that are reflected incoherently from the backside of the sample. The crosses marked as ‘BWO’ in (c) represent the experimental data obtained from the BWO spectrometer.

During cooling, resonances lines are narrowed as damping constants decrease. As a result, the reliability of its separation is increased. The parameters of longitudinal optical phonons have been derived using the classical oscillator model by considering them as zeros in the dielectric function [52]. Errors in the determination of  $\nu_{LO}$  values result from differing damping constants for the transverse and longitudinal modes. If  $\gamma_{TOj} \neq \gamma_{LOj}$ , then calculations using the classical oscillator model either yield the parameters of the transverse mode or an averaged fit over the Reststrahlen band. There is also another factor increasing errors in the calculated spectra of optical phonon modes, namely high-order many-particle processes. The influence of such processes is most pronounced in the high-frequency region of the spectra of the optical phonon modes [57]. Determining the parameters of optical phonons using the factorised four-parameter model allows us to calculate the frequencies and damping constants for both longitudinal and transverse phonons and allows us to distinguish the

contributions of many-particle processes. We used the value of the high-frequency dielectric constant  $\epsilon_{\infty}$  from [58, 59] while accounting for the dispersion in the MIR and near-IR ranges. The parameters of optical phonon modes  $A_2$  and E at temperatures of 77 and 300 K are listed in tables 1 and 2, respectively.

The damping constant ratio of the IR active phonon modes, as determined by the factorised four parameter model, does not follow the Lowndes conditions ( $\gamma_{LOj} \geq \gamma_{TOj}$ ) [27] for the modes  $A_2(2)$ ,  $A_2(4)$ , E(3), or E(6) and E(8). This condition is fulfilled for a single phonon mode pair with a small value of LO-TO splitting. The condition of positive absorption in media with multiple polar-optical phonon modes leads to a generalised expression of the form  $\sum_j (\gamma_{LOj} - \gamma_{TOj}) \geq 0$  [60, 61]. An additional band in the frequency range of LO-TO splitting of the  $A_2(4)$  polar mode can be observed. Factor group analysis reveals the four IR active phonon modes in the [001] direction. This band can be associated with second-order two-phonon

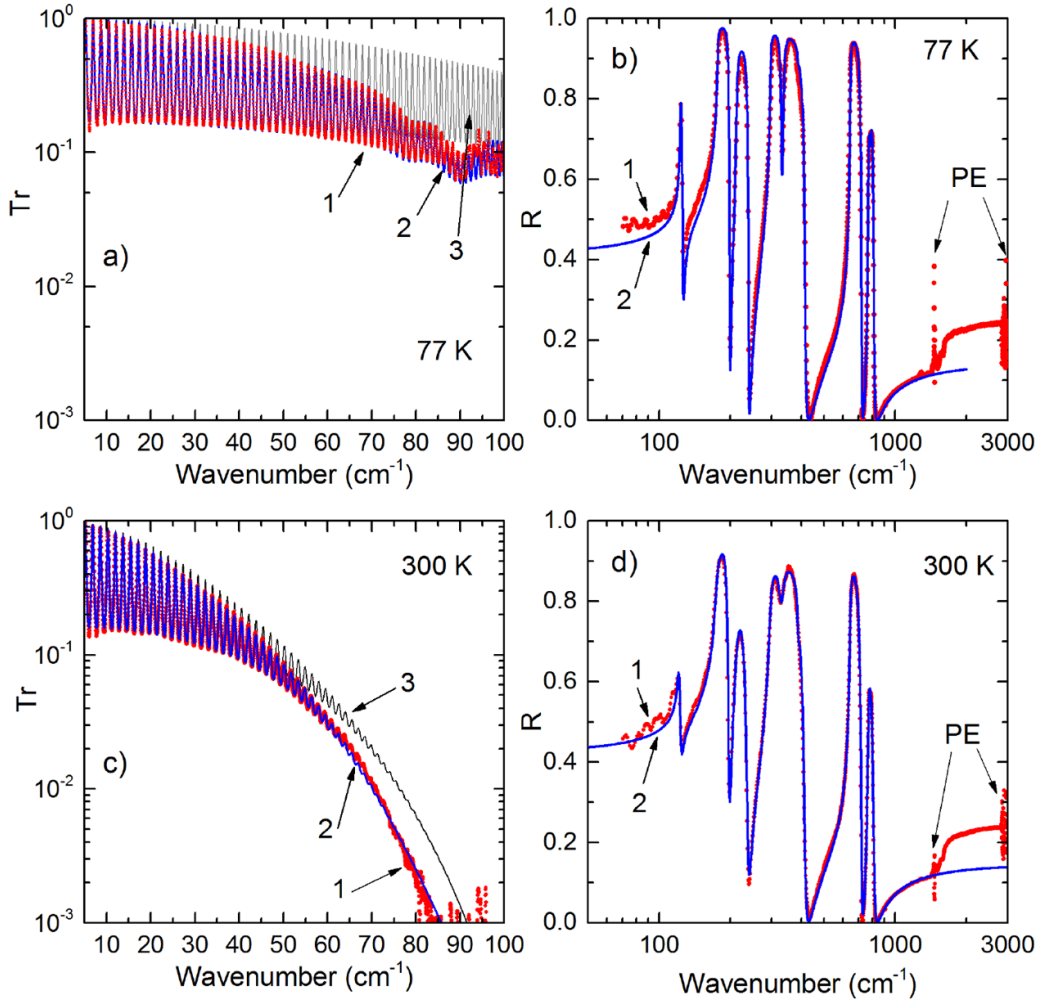


**Figure 2.** (a), (c) Transmissivity and (b), (d) reflectivity spectra of paratellurite single crystals for  $\mathbf{E}||[110]$  at 77 and 300 K. Experimental data: points. Calculation results: lines. The grey lines in (a), (c) were calculated using only the optical phonon mode parameters. The features in the high-frequency region of the spectra have the same origins as those discussed in figure 1.

**Table 1.** Parameters of the IR active optical modes  $A_2$  for  $\alpha\text{-TeO}_2$  [001] ( $\epsilon_\infty = 5.9$ ).

Assignment	T, K	$\nu_{\text{TO}}, \text{cm}^{-1 \text{ a}}$	$\gamma_{\text{TO}}, \text{cm}^{-1 \text{ a}}$	$\nu_{\text{LO}}, \text{cm}^{-1 \text{ a}}$	$\gamma_{\text{LO}}, \text{cm}^{-1 \text{ a}}$	$\Delta\epsilon^{\text{ a}}$	$\nu, \text{cm}^{-1 \text{ b}}$
$A_2(1)$	77	84.6	0.8	110.7	1.2	11.2	90
	300	81.5	2.5	110	3	12.5	
$A_2(2)$	77	262	4.9	271.7	4	1.73	269
	300	260	12	266	10	1.02	
$A_2(3)$	77	320.4	1.1	382.5	6.5	3.97	302
	300	321	6.9	387	7.3	4.05	
$A_2(4)$	77	586.7	7.9	765	7.5	3.12	535
	300	586.7	11.6	772	12.8	3.39	
$\Sigma$	77	655	40	652	40	0.084	640
	300	655	50	653.2	50	0.055	

processes [57]. The use of the four-parameter factorised model for fitting this band inside the LO-TO splitting region of the optical phonon modes yields the peculiarity noted in [62]. In this case, the longitudinal frequency is lower than the transverse frequency of the inserted band according to the requirement of positive absorption. This condition is satisfied for the second-order absorption band  $\Sigma$  in the [001] direction (table 1) and for the E(5) optical phonon mode (table 2).

The temperature dependencies of the low-frequency mode parameters determined using equation (2) are presented in figures 3(a) and (b) for the optical phonon modes  $A_2$  and E, respectively. The temperature dependency of the frequency of the transverse mode  $A_2(1)\text{TO}$  is approximated using the linear law. The frequency of  $A_2(1)\text{TO}$  at the low-temperature limit is approximately  $85 \text{ cm}^{-1}$ . The high-frequency limit of transparency in the THz range for the [001] direction of the

**Table 2.** Parameters of the IR active optical modes E for  $\alpha$ -TeO<sub>2</sub> [110] ( $\epsilon_{\infty} = 4.8$ ).

Assignment	T, K	$\nu_{\text{TO}}$ , cm <sup>-1 a</sup>	$\gamma_{\text{TO}}$ , cm <sup>-1 a</sup>	$\nu_{\text{LO}}$ , cm <sup>-1 a</sup>	$\gamma_{\text{LO}}$ , cm <sup>-1 a</sup>	$\Delta\epsilon$ <sup>a</sup>	$\nu$ , cm <sup>-1 b</sup>
E(1)	77	123	1.3	126	1.82	1.49	123
	300	121	3	123	3.5	1.07	120
E(2)	77	177	1.5	199	1.7	7.75	176
	300	174.6	6.5	197	4.5	8.6	174
E(3)	77	213	3.5	239.5	1.8	2.12	213
	300	210	12.7	237.5	8	2.23	210
E(4)	77	296.5	2.5	387	5.4	3.79	295.2
	300	295	10.2	387	7.6	4.07	294
E(5)	77	334.5	7	331	7	0.28	335
	300	331	19.6	328.4	20	0.24	327.7
E(6)	77	387.05	5.5	415	5	0.0006	—
	300	387.3	8.24	414	10.7	0.004	—
E(7)	77	644.5	4	720	5.4	1.19	643
	300	643	9.4	720	11	1.27	642
E(8)	77	766	7.7	812	7	0.18	767
	300	765	14.3	812	17.8	0.2	766
$\Sigma$	77	784.8	11.5	784	11.7	0.006	784
	300	—	—	—	—	—	—

<sup>a</sup> $\nu_{\text{TO}}$ ,  $\gamma_{\text{TO}}$ ,  $\nu_{\text{LO}}$ , and  $\gamma_{\text{LO}}$  were calculated using equation (2).  $\Delta\epsilon$  was calculated using equation (3).

<sup>b</sup> $\nu$  was calculated using the classical oscillator model (equation (5)) to compare the data from this work to those presented in [52].

crystal does not exceed of 2.5 THz (84 cm<sup>-1</sup>). The temperature behaviour of parameters of the E modes does not follow the simple dependencies. However, upon cooling, the resonant frequencies of both modes remain above 120 cm<sup>-1</sup> and do not affect absorption in the THz range. Therefore, the frequency range of the acousto-optical deflection in the THz range is limited to approximately 80 cm<sup>-1</sup> based on the absorption of radiation by A<sub>2</sub>(1)TO optical phonons. The temperature dependency of the damping constant  $\gamma_{\text{TO}}(T)$  of the A<sub>2</sub>(1)TO phonon mode in the temperature range of 77–300 K can be approximated using the Bose–Einstein model [27, 63]. This is true if the decay rates of the LO and TO phonon modes are independent. Deviations in the temperature dependencies of the  $\gamma_{\text{TO}}(T)$  phonons of the E(1) and E(2) modes from the predicted Bose–Einstein model results may indicate a noteworthy effect of mode coupling on optical phonon lifetimes.

Figures 2(a) and (c) present the transmission spectra in the THz range. Line 3 in parts (a) and (c) represents the spectra calculated using the parameters obtained by fitting Reststrahlen bands in the reflectivity spectra. The differences between the calculated spectra (line 3) and experimental data (line 2) indicate the presence of an additional absorption band in the THz region. This band was modelled using the factorised four-parameter model in equation (2). The contribution to the dielectric permittivity  $\Delta\epsilon_{\text{THz}}$  calculated using equation (3) does not exceed 0.02 and decreases at low temperatures. The simulation results for the entire set of experimental data in the THz and IR ranges are represented in figures 1 and 2 by line 2. The temperature-dependent portion of  $\Delta\epsilon_{\text{THz}}$  is determined by second-order many-particle processes. The absorption line centered near 90 cm<sup>-1</sup> is apparent at low temperatures in the [110] direction. This line is relatively weak and is only reliably revealed in the transmissivity spectrum.

The influence of second-order many-particle processes strongly depends on the nature of the dispersion of phonon branches. The temperature dependencies of different second-order processes can be distinguished from other mechanisms in crystals with a simple cubic lattice, such as MgO [33]. The temperature behaviour of the absorption is non-obvious low-symmetry structures for which the dispersion dependencies of phonon branches facilitate additional types of phonon transitions. For example, the various second-order processes in a beryllium oxide single crystal with a wurtzite structure occur over a wide frequency range and include transitions between optical branches [53]. The dispersion of phonon branches for paratellurite was analysed in [64] and a sufficiently high density of phonon states (DOS) in the THz range was obtained. A significant portion of the DOS is determined by acoustic branches and does not contribute to electro-dipole absorption. The DOS at room temperature in the THz range based on frequency is a smooth function without singularities. The calculated dispersion dependencies of the phonon branches at zone boundaries along directions with high symmetry are characterised by second-order transitions. The energy differences between phonon branches are small, which indicates low cut-off energies for the photons involved in second-order difference processes.

The optical parameters in the THz range were calculated by using the Fresnel formulas for a plane-parallel layer based on the transmission spectra with an interference pattern, which were presented in figures 1(a) and (c), and figures 2(a) and (c). The complex refractive indices in the directions of the ordinary and extraordinary rays were calculated based on interference in a plane-parallel sample. The refractive index and extinction coefficient can be derived in the region of weak dispersion of  $n$  based on the following relationships:

$$n = c/2d\Delta\nu \text{ and } k = -\ln(\text{Tr}_{\text{max}})c/4\pi d\nu_{\text{max}},$$

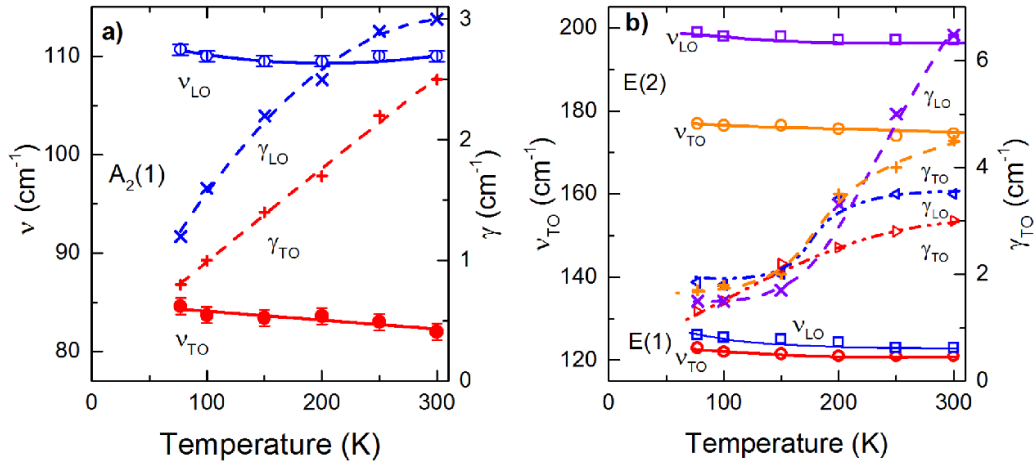


**Figure 3.** Temperature dependencies of the frequencies and damping constants of optical phonons in  $\alpha$ -TeO<sub>2</sub> single crystals. (a) E||[001] for the A<sub>2</sub>(1) mode and (b) E||[110] for the E(1) and E(2) modes. Circles represent the calculated frequencies  $\nu_{TO}$  and  $\nu_{LO}$ . Crosses represent the damping constants  $\gamma_{TO}$  and  $\gamma_{LO}$  determining using equation (2).

where  $d$  is the sample thickness,  $\Delta\nu$  is the frequency difference between adjacent maxima of interference (cm<sup>-1</sup>), and  $Tr_{max}$  and  $\nu_{max}$  are the transmittance coefficient and wavenumber at the interference maxima, respectively. The thermal expansion coefficient of  $\alpha$ -TeO<sub>2</sub> single crystals has a maximum value of approximately 10<sup>-5</sup> K<sup>-1</sup> [65]. In the temperature range of 70–300 K, the change in sample thickness is no more than 1  $\mu$ m, meaning it can be ignored.

The frequency dependencies of the refractive indexes for different temperatures for both polarisations are presented in figure 4. The refractive index increases by approximately 5% as the frequency increases. While cooling from 300 to 77 K,  $n(\nu)$  decreases across the entire spectrum by 2% with no changes in the characteristics of its dispersion, as approximated based on linear dependency. The data presented in the insert in figure 4 highlight the linear dependencies  $n(T)$  for a wavenumber of 20 cm<sup>-1</sup>. Such changes in the temperature behaviour of the dispersion  $n(\nu)$  indicate a decrease in total dielectric permittivity. Assuming that the strengths of the oscillators of the phonon modes are constant, such changes can be attributed to decreases in the contributions of second-order processes.

When cooling from 300 to 77 K, the refractive indexes decrease by 0.15 and 0.1 for the [001] and [110] polarisations, respectively. Considering the small value of the extinction coefficient, the dielectric contributions of the corresponding absorption bands in the THz range decrease during cooling by 0.02 and 0.01, respectively. The data for the changes in the dielectric contributions, as determined by the factorised four-parameter model, are less accurate compared to calculations using the Fresnel formulas. Therefore, to assess changes in the dielectric contributions depending on temperature, we used the results presented in figure 4.

The spectra of the extinction coefficient  $k(\nu)$  are presented in the figure 5. At high temperatures, the extinction coefficient exhibits noticeable dispersion, which is determined by the phonon contribution to absorption. The changes in the spectra  $k(\nu)$  depending on temperature are the same for both

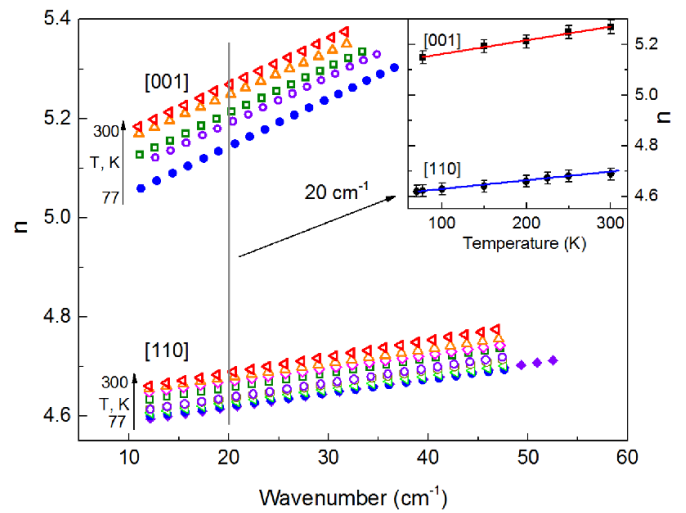


**Figure 4.** Temperature evolution of the refractive index in the THz range. Insert shows the temperature dependence of the refractive index at 20 cm<sup>-1</sup>.

studied crystallographic directions. At low temperatures,  $k(\nu)$  values with good accuracy exhibit dispersion-free behaviour over the shown frequency range. Lattice defects can also affect residual absorption.

Figures 6 and 7 present the generalised dielectric response spectra of paratellurite single crystals, which were constructed from the data obtained at 77 K via TDS and IR spectroscopy. These figures illustrate the contributions to the THz losses of the phonon modes and highlight the additional absorption changes caused by the processes shown in the shaded sections. The frequencies of the maxima in the spectra  $Im(1/\epsilon^*(\nu))$  correspond to the Eigenfrequencies of the longitudinal optical modes. The contribution of each mode to the total dielectric permittivity is estimated based on the value of LO-TO splitting, as depicted by the vertical rectangular bars. The low-frequency portions of the spectra  $\epsilon''(\nu)$  obtained for the temperature of 300 K are presented for comparison

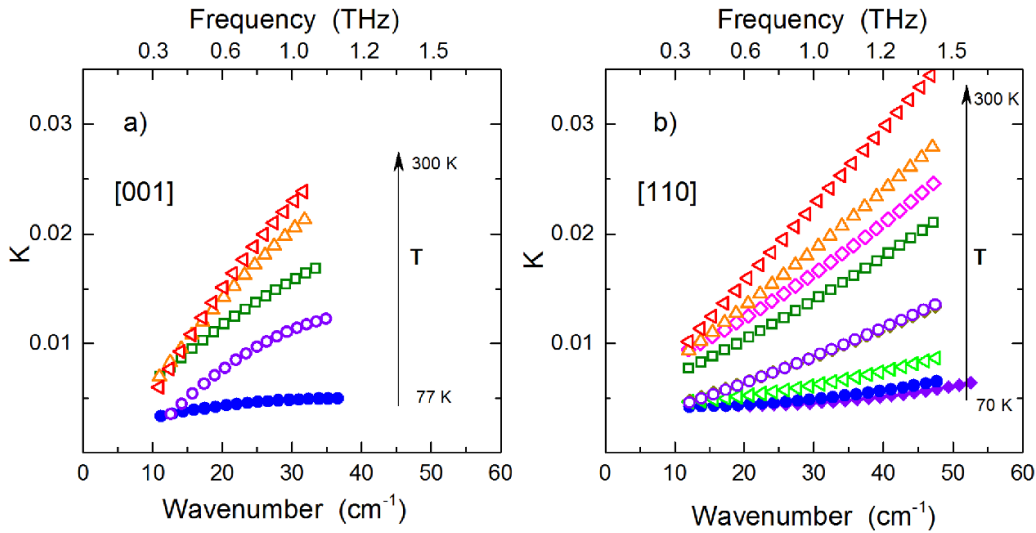


Figure 5. Temperature evolution of the extinction coefficient in the THz range.

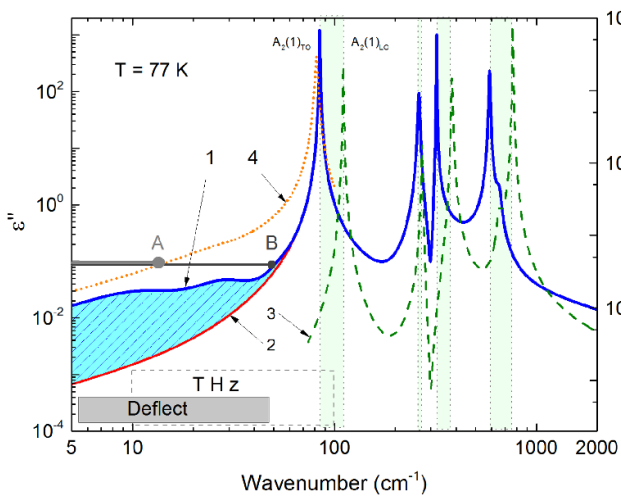


Figure 6.  $\epsilon''(\nu)$  and  $\text{Im}(1/\epsilon(\nu))$  spectra of  $\alpha\text{-TeO}_2$  single crystals in the THz and IR ranges for  $E||[001]$ . Line 1: total spectrum of  $\epsilon''(\nu)$  at 77 K. Line 2: contribution to  $\epsilon''$  of the  $A_2$  optical phonon modes at 77 K. Dashed line 3: spectrum of  $\text{Im}(1/\epsilon(\nu))$  at 77 K. Dotted line 4: spectrum of  $\epsilon''(\nu)$  at 300 K. The vertical bars represent LO-TO splitting of the  $A_2$  optical phonon modes. Point A: high-frequency limit of using  $\alpha\text{-TeO}_2$  for THz beam deflection at 300 K. Point B: same as point A for 77 K. Horizontal bar with dashed border represents the THz range. Bar filled in grey represents the area of deflection at 77 K.

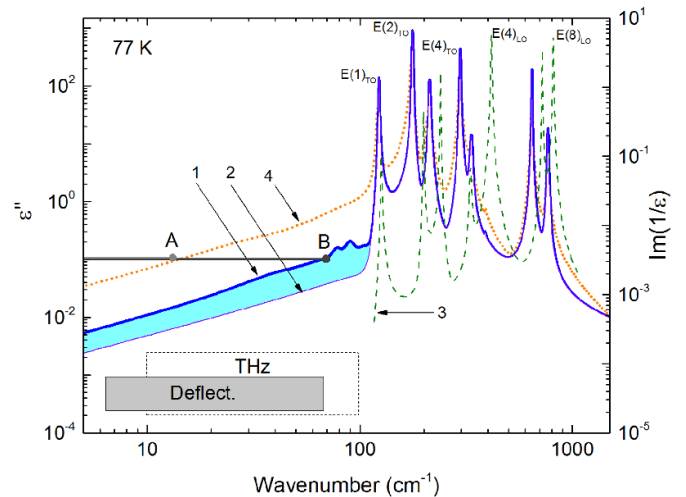


Figure 7.  $\epsilon''(\nu)$  and  $\text{Im}(1/\epsilon(\nu))$  spectra of  $\alpha\text{-TeO}_2$  single crystals in the THz and IR range for  $E||[110]$ . Line 1: total spectrum of  $\epsilon''(\nu)$  at 77 K. Line 2: contribution to  $\epsilon''$  of the E optical phonon modes at 77 K. Dashed line 3: spectrum of  $\text{Im}(1/\epsilon(\nu))$  at 77 K. Dotted line 4: spectrum  $\epsilon''(\nu)$  at 300 K. Point A: high-frequency limit of using  $\alpha\text{-TeO}_2$  for THz beam deflection at 300 K. Point B: same as point A for 77 K. Horizontal bar with dashed border represents the THz range. Bar filled in grey represents the area of deflection at 77 K.

to the low-temperature results. One can see narrowing of the phonon resonance contours and decreasing losses at the high-frequency edge of the THz range caused by second-order processes.

The absorption in the region of the low-frequency dispersion branch was calculated based on the obtained data. Figure 8 presents the results for 300 and 77 K. The frequency dependence of the wave vector  $\mathbf{k}(\nu)$  is obtained from the relationship  $\mathbf{k}(\nu) = 2\pi\nu n(\nu)$ , where  $n(\nu)$  is the real part of the refractive index and the direction of the vector  $\mathbf{k}$  coincides with the [001] direction of the crystal. The spectra

$\alpha(\nu)$  were determined from the modelling parameters. The smooth absorption spectrum at 300 K reveals that a majority of the allowed transitions are involved in the formation of absorption bands in the THz region based on the complete population of acoustic branches. In the region from 30 to 55  $\text{cm}^{-1}$ , two diffuse bands can be observed at 77 K. This may be a result of the transitions between optical branches for which the occupation number is less dependent on temperature.

The material efficiency for the acousto-optical deflection of THz radiation depends on two parameters: the absorption coefficient  $\alpha(\nu)$  and acousto-optical figure of merit  $M_2$ . Bragg

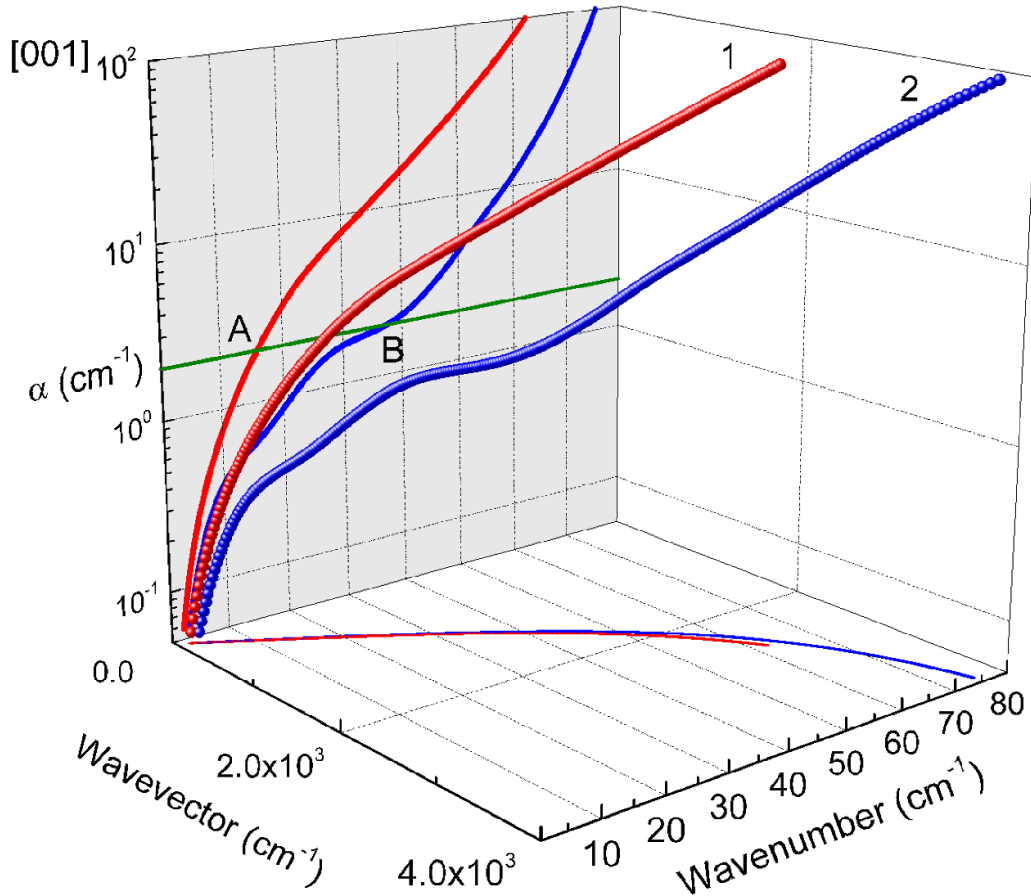


**Figure 8.** Absorption by polaritons in the low-frequency dispersion branch along the [001] direction of  $\alpha$ -TeO<sub>2</sub> single crystals at temperatures of (1) 300 K and (2) 77 K. The absorption level of  $2 \text{ cm}^{-1}$  is indicated by the line in the  $\alpha(\nu)$  plane. Points A and B represent estimations of the high-frequency limits of applicability of this crystal as an element of acousto-optical systems at 300 and 77 K, respectively.

diffraction is the most desirable acousto-optical modulator mode for guiding THz beams. Crystals should have sufficient thickness in the direction of propagation of THz radiation to implement such a regime. The most optimal diffraction pattern for deflection is transverse diffraction [16] with circularly polarised THz waves propagating along the [001] direction and ultrasound waves directed along the [110] direction. The effective length of the acousto-optical interaction  $l$  was determined in [13] based on the absorption coefficient  $l = l/\alpha$ . Assuming the initial interaction length is 0.5 cm, which is a typical value for acousto-optics, the frequency range in which  $\alpha(\nu)$  is less than  $2 \text{ cm}^{-1}$  is acceptable for acousto-optical deflecting. In figure 8, the absorption level of  $2 \text{ cm}^{-1}$  is indicated by a solid line in the  $\alpha(\nu)$  plane. The condition  $\alpha < 2 \text{ cm}^{-1}$  is satisfied for frequencies below approximately  $40 \text{ cm}^{-1}$  at low temperatures, but is only limited to  $15 \text{ cm}^{-1}$  at room temperature. The value of  $M_2$  was estimated in [16] and determined to be much greater than the value of Ge. During cooling, the acousto-optical figure of merit increases based on decreases in the phase velocity of acoustic waves [23]. Additionally, the presented results indicate that absorption in the THz range is significantly weaker than that for Ge, particularly at low temperatures.

#### 4. Conclusion

The main issue restricting the application of paratellurite crystals at room temperature for deflecting THz radiation is large absorption at frequencies above  $15 \text{ cm}^{-1}$  ( $0.45 \text{ THz}$ ). In the THz range, absorption is determined by the sum of various contributions. Extrinsic absorption caused by defects is insignificant and temperature independent. For high-quality crystals, its contribution does not have a noteworthy influence on the efficiency of deflection. We studied the two most significant intrinsic processes in the absorption THz radiation. The first mechanism is the well-known absorption by phonons in the centre of the Brillouin zone. The contribution of this process to absorption at room temperature in paratellurite is dominant. This absorption is determined by the dispersion of the low-frequency tail of  $A_2(1)$ TO optical phonon modes in the [001] direction. Changes of the absorption coefficient with temperature are determined primarily by the decreasing damping coefficients  $\gamma(T)$  of the low-frequency optical phonon modes during cooling. The other types of significant absorption mechanisms are second-order processes. Absorption in the THz region caused by these processes has a direct proportional dependence on temperature, which leads to an increase in the transmittance of crystals during cooling. The

accompanying decrease in the refractive index during cooling is insignificant and amounts to  $\Delta n = n_{300\text{K}} - n_{77\text{K}} \sim 0.2$ , which does not exceed 0.4% of the value of  $n_{300\text{K}} \sim 5.3$ . These changes in the refractive index only slightly affect to the acousto-optical figure of merit. In acousto-optical devices based on paratellurite crystals, electromagnetic waves propagate along the [001] direction. Therefore, there is a fundamental restriction in the THz range caused by the first-order absorption of  $A_2(1)TO$  optical phonon modes with a frequency of approximately  $80\text{ cm}^{-1}$ . Considering all of the absorption mechanisms discussed above, the high-frequency limit for the application of paratellurite as a radiation deflector in the THz range is  $40\text{ cm}^{-1}$  (1.2 THz) at temperatures below 100 K. Therefore, cooling has a positive effect on the operation of this crystal in the Bragg diffraction mode based on a decrease in total absorption, which increases the high-frequency boundary of the acousto-optical application of  $\alpha\text{-TeO}_2$  in the THz range by more than two times. It should be noted that  $\alpha\text{-TeO}_2$  crystals have better acousto-optical properties in terms of the efficiency of deflecting THz beams compared to Ge, but are inferior in terms of their operating frequency range.

## Acknowledgments

This work was partially supported by the Russian Foundation for Basic Research (Grant Nos. 18-32-00322) and by the Ministry of Science and Higher Education within the State Assignment FSRC Crystallography and Photonics RAS as part of 'crystal growth and sample preparation'.

## Disclosures

The authors declare that there are no conflicts of interest regarding the publication of this article.

## ORCID iD

Gennadiy Komandin  <https://orcid.org/0000-0003-1101-8225>

## References

- [1] Chernomyrdin N V et al 2018 *Appl. Phys. Lett.* **113** 111102
- [2] Chernomyrdin N V et al 2017 *Appl. Phys. Lett.* **110** 221109
- [3] Shen Y-C and Taday P F 2008 *IEEE J. Sel. Top. Quantum Electron.* **14** 407
- [4] Guerboukha H, Nallappan K and Skorobogatiy M 2018 *Adv. Opt. Photonics* **10** 843
- [5] Markl D et al 2017 *J. Pharm. Sci.* **106** 1586
- [6] Wan M, Healy J J and Sheridan J T 2020 *Opt. Laser Technol.* **122** 105859
- [7] Son J-H, Oh S J and Cheon H 2019 *J. Appl. Phys.* **125** 190901
- [8] Wang D and Xia J 2019 *J. Phys. D: Appl. Phys.* **125** 191101
- [9] Gavadush A A et al 2019 *J. Biomed. Opt.* **24** 027001
- [10] Wang S and Zhang X-C 2004 *J. Appl. Phys.* **37** R1
- [11] Dolganova I N et al 2015 *Rev. Sci. Instrum.* **86** 113704
- [12] Nikitin P, Voloshinov V, Gerasimov V and Knyazev B 2015 *Acta Phys. Pol. A* **127** 49
- [13] Voloshinov V B et al 2013 *Quantum Electron.* **43** 1139
- [14] Unferdorben M et al 2016 *J. Infrared Millim. Terahertz Waves* **37** 703
- [15] Sotome M, Kida N, Takeda R and Okamoto H 2014 *Phys. Rev. A* **90** 033842
- [16] Porokhovnichenko D L et al 2017 *Phys. Wave Phenom.* **25** 114
- [17] Champarnaud-Mesjard J C et al 2000 *J. Phys. Chem. Solids* **61** 1499
- [18] Kondratyuk I P, Muradyan L A, Pisarevskii Y V and Simonov V I 1987 *Crystallogr. Rep.* **32** 609 (in Russian)
- [19] Thomas P A 1988 *J. Phys. C: Solid State Phys.* **21** 4611
- [20] Ohmachi Y and Uchida N 1970 *J. Appl. Phys.* **41** 2307
- [21] Zhi-gong S et al 1992 *Phys. Rev. B* **45** 12834
- [22] Arlt G and Schewpe H 1968 *Solid State Commun.* **6** 783
- [23] Silvestrova I M et al 1981 *Phys. Status Solidi A* **66** K55
- [24] Gurevich V L and Tagantsev A K 1991 *Adv. Phys.* **40** 719
- [25] Chuchupal S V et al 2014 *Phys. Solid State* **56** 1391
- [26] Chuchupal S V et al 2015 *Phys. Solid State* **57** 1607
- [27] Gervais F and Piriou B 1974 *J. Phys. c: Solid State Phys.* **7** 2374
- [28] Barker A S and Hopfield J J 1964 *Phys. Rev.* **135** A1732
- [29] Singh A et al 2018 *ACS Photonics* **5** 2718
- [30] Eldridge J E and Staal P R 1977 *Phys. Rev. B* **16** 4608
- [31] Stolen R and Dransfeld K 1965 *Phys. Rev.* **139** A1295
- [32] Sparks M, King D F and Mills D L 1982 *Phys. Rev. B* **26** 6987
- [33] Komandin G A, Porodinkov O E, Spector I E and Volkov A A 2009 *Phys. Solid State* **51** 2045
- [34] Komandin G A et al 2009 *Phys. Solid State* **51** 1351
- [35] Komandin G A et al 2014 *Phys. Solid State* **56** 2206
- [36] Komandin G A et al 2017 *Phys. Status Solidi C* **14** 1600211
- [37] Kozlov G and Volkov A 1998 *Coherent source submillimeter wave spectroscopy Millimeter and Submillimeter Wave Spectroscopy of Solids* vol 74 (Berlin: Springer) (<https://doi.org/10.1007/BFb0103420>)
- [38] Komandin G A et al 2013 *IEEE Trans. Terahertz Sci. Technol.* **3** 440
- [39] Komandin G A et al 2019 *Opt. Spectrosc.* **126** 514
- [40] Volkov A A et al 1982 *Int. J. Infrared Millim. Waves* **3** 19–43
- [41] Komandin G A et al 2019 *Opt. Eng.* **59** 061603
- [42] Lyddane R H and Herzfeld K F 1938 *Phys. Rev.* **54** 846
- [43] Lyddane R H, Sachs R G and Teller E 1941 *Phys. Rev.* **59** 673
- [44] Kurosawa T 1961 *J. Phys. Soc. Jpn.* **16** 1298
- [45] Berreman D W and Unterwald F C 1968 *Phys. Rev.* **174** 791
- [46] Gervais F and Piriou B 1974 *Phys. Rev. B* **10** 1642
- [47] Schöche S et al 2013 *J. Appl. Phys.* **113** 164102
- [48] Merten L and Lamprecht G 1970 *Phys. Status Solidi* **39** 573
- [49] Servoin J L, Luspain Y and Gervais F 1980 *Phys. Rev. B* **22** 5501
- [50] Kukharskii A A 1976 *Opt. Spectrosc.* **41** 499 in Russian
- [51] Gervais F 1983 *Infrared and Millimeter Waves Edition* vol 8 (New York: Academic) pp 279–339
- [52] Korn D M, Pine A S, Dresselhaus G and Reed T B 1973 *Phys. Rev. B* **8** 768
- [53] Komandin G A et al 2015 *Phys. Solid State* **57** 2389
- [54] Nyquist H 1928 *Trans. Am. Inst. Electr. Eng.* **47** 617
- [55] Kotel'nikov V A 2006 *Phys. Usp.* **49** 736
- [56] Shannon C E 1948 *Bell Syst. Tech. J.* **27** 379
- [57] Burstein E, Johnson F A and Loudon R 1965 *Phys. Rev.* **139** A1239
- [58] Karaman M I, Lichman V A, Mushinskii V P and Smirnov Y M 1988 *J. Appl. Spectrosc.* **49** 1188
- [59] Uchida N 1971 *Phys. Rev. B* **4** 3736
- [60] Lowndes R P 1970 *Phys. Rev. B* **1** 2754
- [61] Schubert M, Tiwald T E and Herzinger C M 2000 *Phys. Rev. B* **61** 8187
- [62] Baumard J-F and Gervais F 1977 *Phys. Rev. B* **15** 2316
- [63] Knight S et al 2020 *J. Appl. Phys.* **127** 125103
- [64] Ceriotti M, Pietrucci F and Bernasconi M 2006 *Phys. Rev. B* **73** 104304
- [65] Uchida N and Ohmachi Y 1969 *J. Appl. Phys.* **40** 4692